nature communications

Article

https://doi.org/10.1038/s41467-025-60954-4

A layered lead halide framework intercalated with $Ru(bpy)_3$ for efficient CO_2 photoreduction

Received: 2 December 2024

Accepted: 10 June 2025

Published online: 01 July 2025

Check for updates

Yilin Jiang[1,3], Ruonan Xi[1,2,3], Jinlin Yin[1], Chen Sun[1], Yukong Li[1], Chao Wu[1], Chi Zhang[1] ✉ & Honghan Fei[1] ✉

Three-dimensional lead halide hybrids exhibit excellent photophysical properties but suffer from inherent instability. In contrast, two-dimensional layered lead halides offer enhanced environmental stability, yet their strongly bound excitons restrict efficient charge transport. Here we present a covalent intercalation strategy involving the benchmark photosensitizer $[Ru(bpy)_3]^{2+}$ into a layered lead halide framework, featuring cationic $[Pb_{23}X_{42}]^{4+}$ ($X^- = Cl^-$ or Br^-) layers pillared by $[Ru(bpy)_3]^{2+}$ ligands via Pb^{2+}-carboxylate coordination. This hybrid material achieves nearly full visible-light absorption and efficient photoinduced charge transfer from $[Ru(bpy)_3]^{2+}$ to the lead halide layers. This affords efficient CO_2-to-CO photoreduction with an apparent quantum efficiency of ~3.0% at 500 nm, exceeding the performance of all previously reported organolead halide photocatalysts. Mechanistic studies indicate that the $[Ru(bpy)_3]^{2+}$ ligands enhance charge transport to Pb^{2+} sites, facilitating CO_2 activation and reducing the reaction barrier for the *COOH intermediate. This work establishes a paradigm for intercalation chemistry in robust layered lead halide hybrids.

Lead halide hybrids have garnered significant attention in recent years owing to their excellent structural tunability and remarkable photophysical properties[1–3]. Among these, 3D lead halide hybrids have emerged as the state-of-the-art photovoltaic materials, exhibiting optoelectronic characteristics such as broad visible-light absorption, efficient charge transport and long carrier lifetime[4–6], despite their inherent moisture and thermal instability[7,8]. In contrast, quasi-2D layered lead halides, featuring lead halide layers separated by the organic component, represent a class of photoactive materials with enhanced stability[9,10]. However, these quasi-2D structures, typically with large interlayer spacings, do not exhibit the superior light-harvesting behaviors that are associated with the 3D counterpart[11,12]. As a result, they tend to have larger bandgaps and narrower absorption ranges[13–15]. Although efforts have been made to increase the layer thickness to enhance their visible-light absorption, there remains a strong demand and challenge in intercalation of light-harvesting antenna to chemically functionalize layered lead halides[16].

Our group focuses on coordination-driven assembly of lead halide frameworks utilizing organocarboxylate ligands[17]. Unlike the ionic structures of conventional lead halide hybrids, the coordination-assembly strategy affords the coordination polymers with high intrinsic stability, maintaining structural integrity over a wide range of pH as well as aqueous boiling condition[18–22]. Moreover, the covalent Pb^{2+}-carboxylate interactions between inorganic and organic components hold high potential to enhance inherent charge transfer properties within the materials[23,24]. Therefore, this class of lead halide frameworks exhibits excellent carrier transport characteristics for photocatalysis, such as long carrier lifetime and μm-ranged carrier diffusion length[19,24]. However, the spatial separation of lead halide units by carboxylate linkers results in a large bandgap and narrow absorption wavelength coverage

[1]School of Chemical Science and Engineering, Shanghai Key Laboratory of Chemical Assessment and Sustainability, Tongji University, Shanghai, P. R. China. [2]Analysis and testing center, Southeast University, Nanjing, P. R. China. [3]These authors contributed equally: Yilin Jiang, Ruonan Xi.
✉e-mail: chizhang@tongji.edu.cn; fei@tongji.edu.cn

for these lead halide frameworks, which limits their utilization of visible light for photocatalysis[25]. To overcome this limitation, the incorporation of an efficient light-harvesting antenna (*e.g.*, $[Ru(bpy)_3]^{2+}$) into the lead halide frameworks will be an effective and promising strategy.

$[Ru(bpy)_3]^{2+}$ (bpy=2,2′-bypyridine) complexes are a well-established family of photosensitizers known for their exceptional light-harvesting properties and broad absorption coverage spanning the visible range[26]. Moreover, $[Ru(bpy)_3]^{2+}$-based derivatives possess excellent photophysical properties, including a long excited-state lifetime that promotes efficient charge transfer and separation processes[27]. These unique characteristics make $[Ru(bpy)_3]^{2+}$-based molecules ideal candidates for various applications, such as solar cells, photocatalysis, and light-emitting devices[28–30]. Indeed, $[Ru(bpy)_3]^{2+}$ complexes have widespread uses as homogeneous photosensitizers in photocatalytic reactions, such as CO_2 photoreduction, hydrogen production, and water oxidation[31–34]. The functionalization of $[Ru(bpy)_3]^{2+}$ have been studied in a variety of solid-state materials, including metal-organic frameworks (MOFs), metal oxide, and zeolites, resulting in enhanced light-harvesting behavior and the visible-light photocatalytic activity[35–37]. Particularly, the $[Ru(bpy)_3]^{2+}$-functionalized MOFs have demonstrated an efficient ligand-to-metal charge transfer (LMCT) process from $[Ru(bpy)_2(dcbpy)]^{2+}$ (dcbpy = 2,2′-bipyridyl-5,5′-dicarboxylic acid) to catalytically active metal sites for enhanced photocatalysis[38]. Up-to-date, it still remains a great challenge to realize the $[Ru(bpy)_3]^{2+}$-functionalized lead halides by crystal engineering, especially achieving the efficient photoinduced charge transfer through coordination assembly.

Herein, we present the successful synthesis of a layered lead halide framework intercalated with $[Ru(bpy)_3]^{2+}$ complexes, where the $[Ru(H_2dcbpy)_3]^{2+}$ ligands act as interlamellar pillars connecting the cationic $[Pb_{23}X_{42}]^{4+}$ ($X^- = Cl^-$ or Br^-) layers through Pb^{2+}-carboxylate bonding. Compared to a control layered lead halide framework pillared by 1,4-cyclohexanedicarboxylate (chdc)[20], our $Ru(bpy)_3$-intercalated lead halide ($X^- = Cl^-$ or Br^-) significantly extends its absorption edge to 680 nm, covering nearly the entire visible-light range. Comprehensive photophysical studies, including steady-state and transient-state PL studies and surface photovoltage spectroscopy (SPV), confirm an efficient LMCT process from $[Ru(Hdcbpy)_3]^-$ ligands to Pb^{2+} centers, facilitating the fast charge transport along the lead halide layers. The synergistic interaction between lead halide layers and the $Ru(bpy)_3$ photosensitizer enables efficient photocatalytic CO_2 reduction to CO, achieving a high evolution rate of 11.81 μmol h^{-1} with 30 mg of photocatalysts and an apparent quantum efficiency (AQE) of 3.0 % at 500 nm. This performance surpasses those of most hybrid lead halides and far exceeds that of a physical mixture of $[Ru(bpy)_3]Cl_2$ with a control material without $Ru(bpy)_3$ functionalization. The photocatalytic mechanism suggests the Pb^{2+} centers as the major active sites, which effectively stabilizes the *COOH intermediate to promote efficient CO_2-to-CO photoreduction.

Result and discussion

Synthesis and crystal structures

First, the layered lead halide framework pillared by photochemically inert chdc ligand (chdc= 1,4-cyclohexanedicarboxylate) was synthesized by solvothermal reaction of $PbBr_2$ and $chdcNa_2$ in a mixed solution of deionized water and hydrobromic acid, affording colorless platelike crystals of $Pb_2Br_2(chdc)$ (TJU-11, TJU=Tongji University) (Fig. 1 top)[20]. To extend visible light absorption coverage in these layered lead halide frameworks, the $[Ru(H_2dcbpy)_3]\cdot Cl_2$ ligand, featuring the benchmark $[Ru(bpy)_3]^{2+}$ light-harvesting antenna moieties, was synthesized with slight modifications based on the literature (Fig. S1)[39]. Single crystals of the $[Ru(H_2dcbpy)_3]\cdot Cl_2$ ligands were obtained through hydrothermal reaction of $RuCl_3\cdot 3H_2O$ and 2,2′-bipyridine-4,4′-dicarboxylic acid in an aqueous solution of hydrochloric acid and structurally characterized by X-ray crystallography (Fig. S2

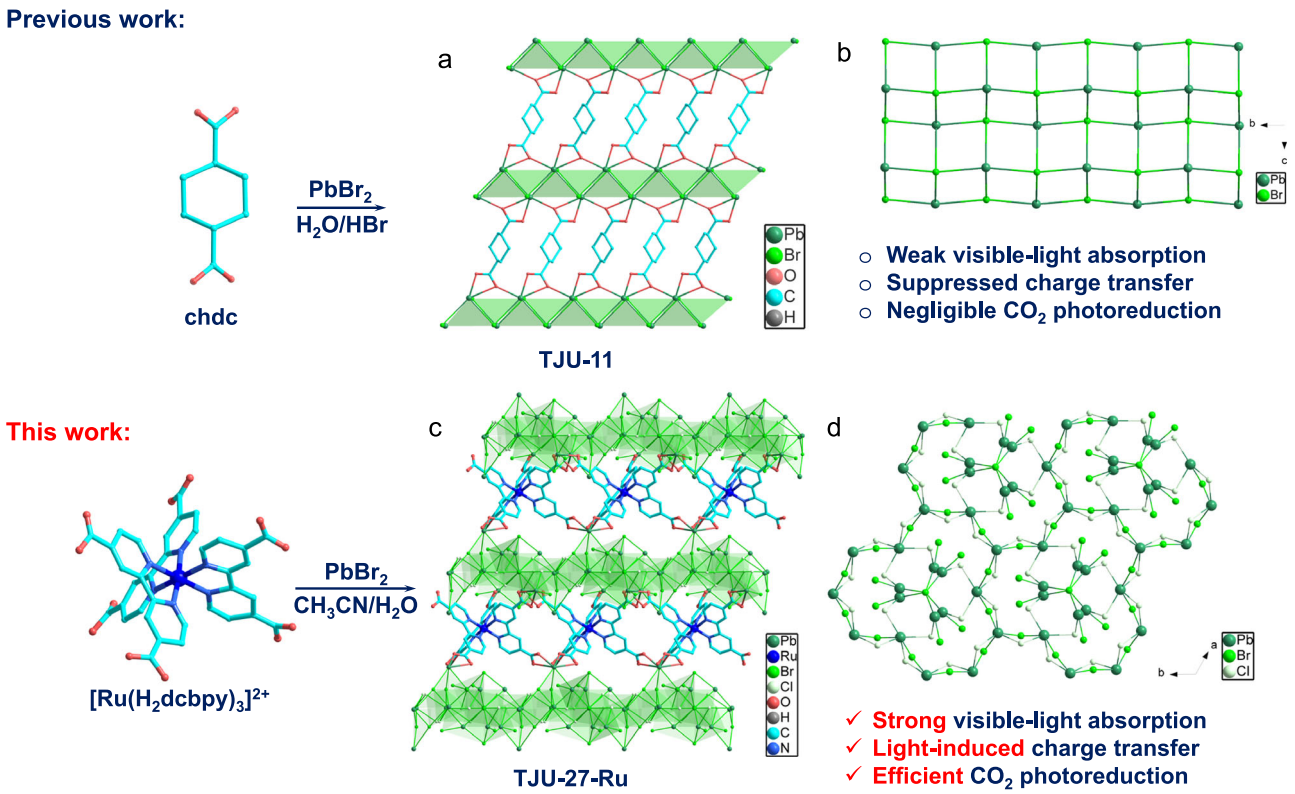

Fig. 1 | Synthetic scheme of TJU-11 and TJU-27-Ru. a Crystallographic view of TJU-11 along the *b*-axis. **b** Crystallographic top-view of a single $[Pb_2Br_2]$ sheet. **c** Crystallographic view of TJU-27-Ru along *b*-axis. **d** Crystallographic cross-sectional view of a single $[Pb_{23}Br_{31.28}Cl_{10.8}]$ sheet. Green polyhedra represent the coordination spheres of Pb^{2+} centers.

and Table S1). Solvothermal reaction between $PbBr_2$ and $[Ru(H_2dcbpy)_3]\cdot Cl_2$ in a CH_3CN/H_2O mixture produced dark-red, plate-like crystals of $[Pb_{23}Br_{31.2}Cl_{10.8}]^{4+}[Ru(Hdcbpy)_3^-]_4$ (TJU-27-Ru) (Fig. 1 bottom, Figs. S3 and S4). Single-crystal crystallography revealed that TJU-27-Ru crystallizes in the trigonal crystal system, adopting the non-centrosymmetric space group *R*32 (Table S2). This space group is characterized by six symmetry elements (E, $2C_3$, $3C_2$), and belongs to the point group 32. Powder second harmonic generation (SHG), a reliable method for probing the symmetry of crystal structures, exhibited an SHG intensity of ~0.25 KTP ($KTiOPO_4$) at 1500 nm and confirmed the non-centrosymmetric nature of TJU-27-Ru (Fig. S5)[40,41]. Moreover, the SHG intensities of TJU-27-Ru increase with particle size, suggesting its phase-matching behavior (Fig. S6).

The overall structure consists of cationic $[Pb_{23}Br_{31.28}Cl_{10.8}]^{4+}$ layers that are pillared by the partially deprotonated $[Ru(Hdcbpy)_3]^+$ ligands residing in the interlamellar region (Fig. 1c). For each H_2dcbpy unit in the $[Ru(bpy)_3]$-based ligands, one carboxylate group becomes deprotonated and coordinates with Pb^{2+} upon incorporation into the layered structure, while the other carboxyl group remains protonated. This was further confirmed by Fourier transform infrared spectroscopy (FT-IR), which showed a notable decrease and red shift in the carbonyl stretching frequency of ~1718 cm^{-1} for $[Ru(H_2dcbpy)_3]\cdot Cl_2$ and the appearance of a new carbonyl band at ~1574 cm^{-1} for TJU-27-Ru (Fig. S7). The Br^- from the $PbBr_2$ precursor and the Cl^- counter-anion from the $[Ru(H_2dcbpy)_3]\cdot Cl_2$ ligand together render a mixed halide composition in the cationic triple layers with an overall stoichiometry of $[Pb_{23}Br_{31.28}Cl_{10.8}]^{4+}$ (Fig. 1d). The four crystallographic independent Pb^{2+} centers exhibit distinct coordination environments, with two located in the center layer and two in the outer sheets. In the center layer, a planar $[Pb_4BrCl_{11}]^{4-}$ sheet is formed, involving two Pb^{2+} centers coordinated by six halogen atoms (Figs. S8, S9). The two outer surface layers feature two other crystallographic independent Pb^{2+} centers with asymmetric geometries. One of these Pb^{2+} centers is in a six-coordinate environment with three Br^- anions and three carboxylate oxygens from three ligands. The other Pb^{2+} is also six-coordinate with three Br^- anions, one Cl^- anion, and two carboxylate oxygens from a single ligand. The triple-layered configuration of the cationic $[Pb_{23}X_{42}]^{4+}$ ($X^- = Cl^-$ or Br^-) slab results in a substantial layer thickness of approximately 10.9 Å, higher than our previous lead halide carboxylate frameworks (Fig. S10)[20,22]. This increased layer thickness is widely recognized as advantageous for enhanced carrier transport in layered lead halides, which will be discussed in detail later[11,42].

TJU-27-Ru was synthesized with high yield and high phase purity on a single-batch gram scale, as confirmed by C/H/N elemental analysis (calc. C 15.75%, H 0.77%, N 3.06%; obs. C 16.05%, H 0.72%, N 3.10%). The phase purity was further supported by the good agreement between experimental powder X-ray diffraction (PXRD) patterns and the simulated pattern based on single-crystal X-ray data (Fig. S11). Thermogravimetric analysis (TGA) and ex-situ thermodiffraction indicated high thermal stability up to 200 °C in air (Figs. S12, S13). Notably, TJU-27-Ru exhibited excellent chemical robustness across a wide range of polar solvents, including isopropanol, acetone, methanol, ethanol, and even aqueous conditions. This was evidenced by the PXRD patterns collected after incubating the as-synthesized TJU-27-Ru crystals in these solvents for 24 h (Fig. 2a). The high stability of the lead halide framework outperforms conventional layered lead halide perovskites, primarily due to high structural integrity of Pb^{2+}-carboxylate coordination between lead halide layers and $Ru(bpy)_3$-based ligands. The high photostability of TJU-27 was further studied by continuous light irradiation (300 W Xe lamp, 24 W cm^{-2}) for 48 h at room temperature (Fig. S14). Overall, these stability tests demonstrate that TJU-27-Ru is a potentially robust photocatalytic platform suitable for CO_2 photoreduction.

Band Structures

We continue to employ both spectroscopic studies and theoretical calculations to investigate the electronic band structure of TJU-27-Ru. Ultraviolet-visible (UV-vis) diffuse reflectance spectroscopy revealed a significant red-shift in the absorption edge of TJU-27-Ru compared to

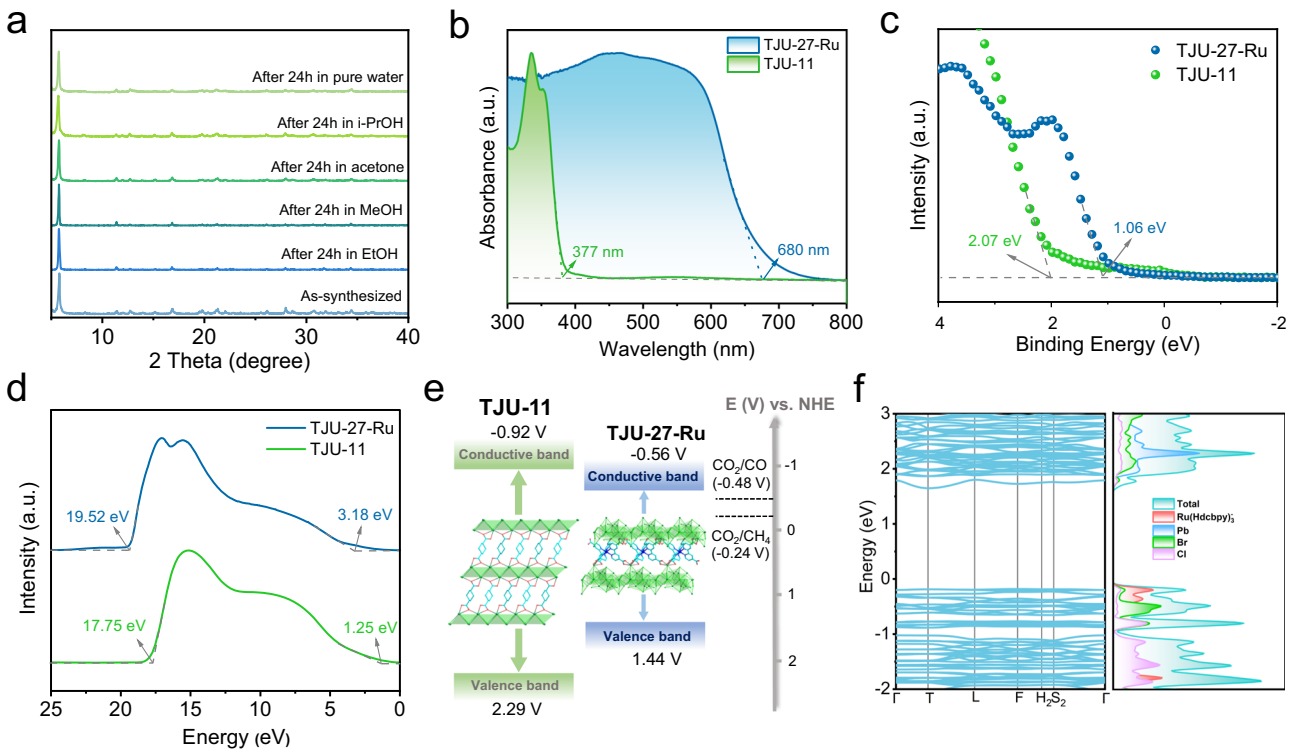

Fig. 2 | PXRD and band structures of TJU-27-Ru and TJU-11. a PXRD of TJU-27-Ru before and after chemical treatment. **b** UV–Vis diffuse reflectance spectroscopy of TJU-27-Ru and TJU-11. **c** VB-XPS spectra of TJU-27-Ru and TJU-11. **d** UPS spectra of TJU-27-Ru and TJU-11. **e** Schematic band structure diagram for TJU-27-Ru and TJU-11. **f** Calculated band structure and DOS of TJU-27-Ru. Source data are provided as a Source Data file.

TJU-11, extending up to approximately 680 nm and thus the absorption covering almost the entire UV-visible range (Fig. 2b). Using the Kubelka-Munk method, the bandgap energies (E_g) were calculated from Tauc plot as 2.00 eV for TJU-27-Ru and 3.21 eV for TJU-11 (Figs. S15, S16). The lower bandgap of TJU-27-Ru enhances the ability to harness a broader spectrum of visible light, which is attributed to the incorporation of $Ru(bpy)_3$-based ligands and the increased thickness of the cationic lead halide layers. To further understand their electronic band positions, we investigated the energy band positions by performing a combination of ultraviolet photoelectron spectroscopy (UPS) and valence band X-ray photoelectron spectroscopy (VB-XPS). As shown in Fig. 2c, d, the valence band maxima (VBM, vs. vacuum) were found to be 5.94 eV for TJU-27-Ru and 6.79 eV for TJU-11. After conversion to electrochemical potential energies, the VBM (vs. NHE) were determined to be 1.44 V for TJU-27-Ru and 2.29 V for TJU-11. Consequently, the conduction band minima (CBM, vs. NHE, at pH 7) were calculated to be −0.56 V for TJU-27-Ru and −0.92 V for TJU-11. Moreover, Mott-Schottky measurements were conducted to determine the flat-band potential of TJU-27-Ru, rendering a flat-band potential of −0.71 V (−0.51 V vs. NHE, at pH 7) relative to the Ag/AgCl electrode (Fig. S17). Given that the CBM of an *n*-type semiconductor is typically 0.1 ~ 0.3 V more negative than the flat-band potential[43], the CBM of TJU-27-Ru was estimated to be ~−0.61 V vs. NHE, which is consistent with the UPS data. Overall, the band structure analysis confirms that both TJU-11 and TJU-27-Ru possess thermodynamically favorable electronic configurations for photocatalytic CO_2 reduction (Fig. 2e).

The band structure of TJU-27-Ru was further investigated by DFT calculations, which revealed an indirect bandgap of 1.83 eV with CBM and VBM positioning at the T point and the F point, respectively, in good agreement with the experimental value of 2.00 eV (Fig. 2f). The total density of states (DOS) and the projected density of states (pDOS) on Pb, Br, Cl, Ru and N orbitals suggest that CBM is primarily composed of Pb *6p* orbitals, while $[Ru(Hdcbpy)_3]^+$ ligands significantly contribute to VBM (Fig. 2f). Importantly, the involvement of carboxylates to the frontier orbitals suggest the covalent nature of the Pb^{2+}-carboxylate coordination motif, which facilitates the potential charge transfer between the Pb^{2+} centers and $[Ru(Hdcbpy)_3]^+$ ligands (Fig. S18). These results indicate that the intercalation of $Ru(bpy)_3$ ligands into the layered lead halide plays a crucial role in modulating the electronic structure near the valence band. This, in turn, enhances the efficiency of photoinduced charge transfer from the $Ru(bpy)_3$ centers to the haloplumbate layers.

Photocatalytic CO_2 reduction

Photocatalytic CO_2 reduction experiments were first conducted under AM1.5 G simulated sunlight irradiation. The gas-phase and liquid-phase products were quantified by gas chromatography (GC) and nuclear magnetic resonance spectroscopy (^{1}H NMR), respectively. Using H_2O as the electron donor, TJU-27-Ru (30 mg) demonstrated CO_2 photoreduction without the need for adding additional photosensitizers or sacrificial agents, primarily producing CO at an evolution rate of 0.75 μmol h^{-1} and CH_4 at a rate of 0.08 μmol h^{-1} (Fig. S19). In addition, when 1,3-dimethyl-2-phenyl-2,3-dihydro-1H-benzo[d]imidazole (BIH) was introduced as a hole trapping agent, the CO_2 photoreduction performance of TJU-27-Ru was significantly enhanced, achieving an impressive CO generation rate of 11.81 μmol h^{-1} and a CH_4 generation rate of 0.31 μmol h^{-1} over a 4 h illumination period (Fig. 3a, Fig. S20, S21). No liquid products were detected in the solution after photocatalysis, evidenced by ^{1}H NMR spectra. TJU-27-Ru exhibited high CO selectivity, reaching 90.5% (product basis) during photocatalytic CO_2 reduction.

Control experiments confirmed that no CO was released in the absence of the photocatalyst (only BIH), CO_2 or light (Fig. 3b), highlighting their essential roles in the photocatalytic process. Furthermore, no significant decrease in CO evolution was observed over three consecutive cycles of continuous light irradiation (12-hours total, with evacuation every 4 h), indicating the long-term stability of our $Ru(bpy)_3$-intercalated lead halide framework (Fig. 3c). Post-photocatalysis PXRD, FT-IR, SEM and XPS revealed that the catalyst retained its high phase purity and crystallinity for multi-cycle photocatalysis, further confirming the excellent stability and durability of TJU-27-Ru for CO_2 photoreduction (Figs. S22, S23, S24, S25). We evaluated the metal leaching from the reaction solution after photocatalysis, showing minimal Pb^{2+} leaching (~1.2%) and a low degree of Ru^{2+} leaching (~3.5%) under reaction conditions. To further mitigate environmental impact, post-catalysis treatment with a natural clay adsorbent (montmorillonite) effectively reduced the Pb^{2+} concentration to meet the lead-containing wastewater discharge standards (1 ppm). Importantly, TJU-27-Ru retained its photocatalytic activity over an extended 24-hours continuous irradiation perid (Fig. S26). Isotope-labeling experiments using $^{13}CO_2$, alongside control experiments under N_2 environment instead of CO_2, confirmed that the carbon in the CO product originated from $^{13}CO_2$ instead of other carbon-related products, as evidenced by the *m/z* signal peak at 29, corresponding to ^{13}CO (Fig. 3d). The wavelength-dependent apparent quantum efficiencies (AQEs) followed the trend of the UV-visible diffuse reflectance spectra, demonstrating that the photocatalytic activity of TJU-27-Ru is primarily driven by the photogenerated carriers (Fig. 3e). Under 500 nm monochromatic light, TJU-27-Ru achieved an impressive AQE of 3.04 % (500 nm) for CO production (Fig. 3e). Moreover, the overall photocatalytic CO_2 reduction performance of TJU-27-Ru surpasses that of all previously reported single-component hybrid lead halides, and even outperforms heterojunction and encapsulation composites based on hybrid lead halides (Fig. 3h)[44–61].

To explore a more practical approach for CO_2 photoreduction, we further utilized natural sunlight to access the photocatalytic performance of TJU-27-Ru. The photocatalytic reaction was performed under identical conditions, but carried out under the natural sunlight irradiation in the outdoor environment of Tongji campus (Shanghai, China) (Fig. 3f). The photocatalytic reaction was performed daily for four consecutive days from 10:00 a.m. to 14:00 p.m. (Fig. 3g). Importantly, TJU-27-Ru was photocatalytically active for CO_2 photoreduction under these natural light conditions and was indeed weather-dependent. The highest CO yield, reaching 33 μmol, was recorded on Aug 5th, 2024, during sunny weather. These results indicate that our $Ru(bpy)_3$-intercalated lead halide framework holds significant promise for practical applications of artificial photosynthesis.

We continue to perform control photocatalysis experiments under identical conditions to highlight the importance of integrating light-harvesting $Ru(bpy)_3$ species and the catalytically active Pb^{2+} sites in a single framework via covalent bonding. First, the photocatalytic activity of TJU-11 was negligible under the identical conditions (Fig. 3a, Figs. S27 and S28). A physical mixture of TJU-11 with the homogeneous $[Ru(H_2dcbpy)_3]\cdot Cl_2$ ligand displayed significantly lower activity, with a low CO production rate of 0.42 μmol h^{-1} and a negligible CH_4 production rate (0.003 μmol h^{-1}) (Fig. 3b). When the $PbBr_2$ precursor was used as the catalyst, no CO production was observed. To further confirm the critical role of covalently linkage between the photosensitizer and the lead halide layers, we tested a physical mixture of quasi-2D layered perovskite $(C_4H_{14}N_2)[PbBr_4]$ and the homogeneous $[Ru(H_2dcbpy)_3]\cdot Cl_2$ ligand under identical conditions (Fig. 3b and Fig. S29)[62]. The observed activity was significantly lower than TJU-27-Ru, affording a CO generation rate of merely 0.34 μmol h^{-1}. In addition, due to the moisture-sensitive nature of the lead perovskite, the structure underwent substantial degradation after a single photocatalytic cycle (Fig. S30).

To further enhance the photocatalytic activity for CO_2 reduction, we attempted to photodeposit Rh nanoparticles as a co-catalyst using $RhCl_3\cdot 3H_2O$ as the precursor. Inductively coupled plasma-optical emission spectroscopy (ICP-OES) confirmed a Rh loading of 0.64 wt.%, affording $Rh_{0.64}$@TJU-27-Ru (Table S4). Notably, the high

https://doi.org/10.1038/s41467-025-60954-4

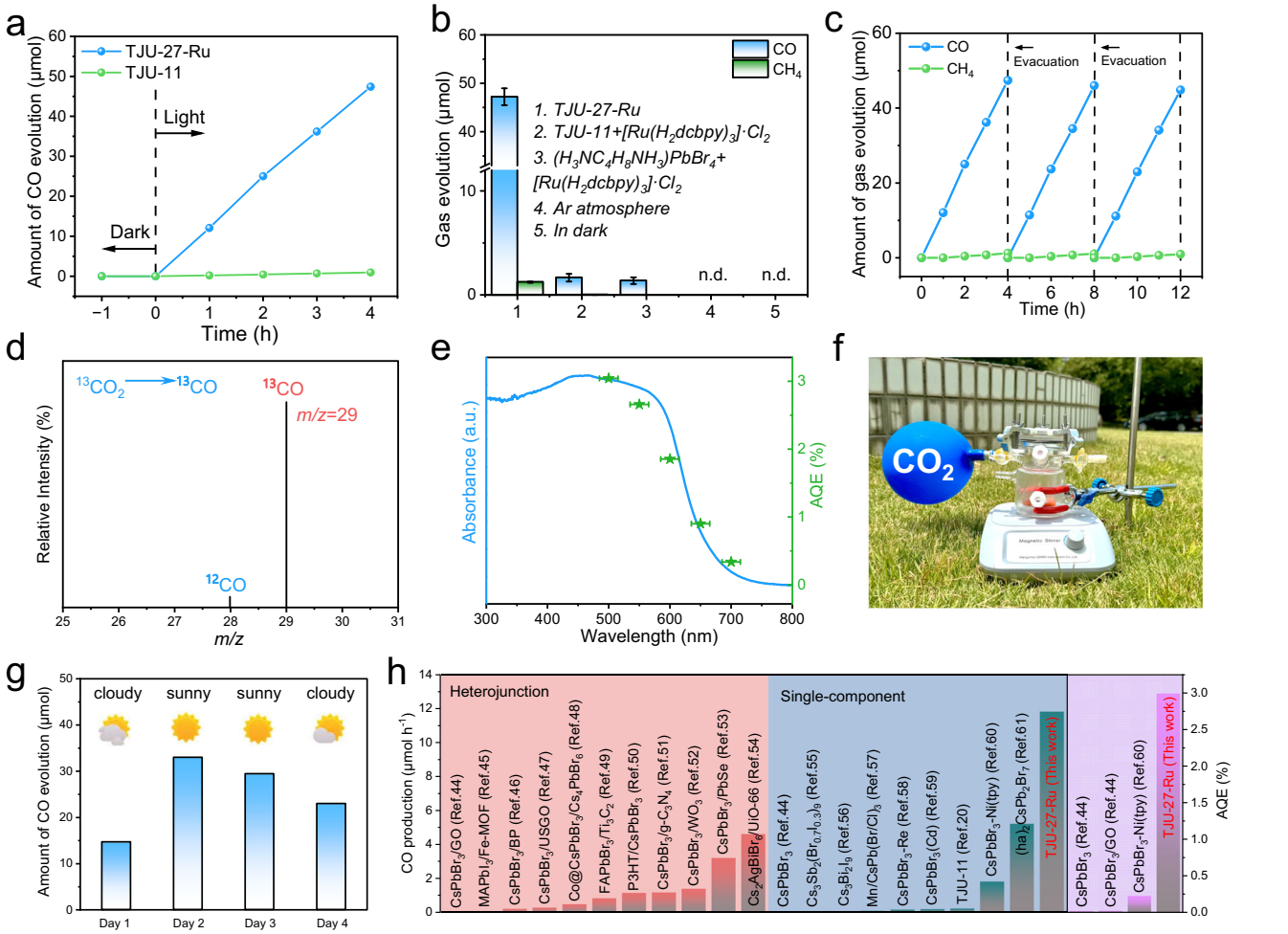

Fig. 3 | Photocatalytic CO_2 reduction performances. a Time courses of CO and CH_4 evolution by photocatalytic CO_2 reduction using TJU-27-Ru and TJU-11 as the photocatalyst upon AM1.5 G irradiation in 5 mL MeCN with 0.1 M BIH. **b** Photocatalytic product evolution of CO and CH_4 based on a 4 h reaction under different catalytic conditions in 5 mL MeCN with 0.1 M BIH. Error bars are based on three independent measurements. **c** Time courses of photocatalytic CO_2 reduction on TJU-27-Ru under AM1.5 G irradiation for 12 h in 5 mL MeCN with 0.1 M BIH, with evacuation every 4 h (dashed line). **d** GC-MS results of ^{13}CO produced over TJU-27-Ru from $^{13}CO_2$ isotope experiment. **e** Wavelength-dependent AQEs of photocatalytic CO_2 reduction on TJU-27-Ru. **f** Experimental device and environment for natural sunlight-driven CO_2 reduction. **g** Natural sunlight-driven CO_2 reduction of TJU-27-Ru in 4 h in 5 mL MeCN with 0.1 M BIH. **h** Comparison of photocatalytic activity of TJU-27-Ru with reported representative metal halides. Source data are provided as a Source Data file.

crystallinity of $Rh_{0.64}$@TJU-27-Ru was well preserved after Rh photodeposition, as evidenced by PXRD (Fig. S31). Under identical photocatalytic conditions, $Rh_{0.64}$@TJU-27-Ru achieved a total CO yield of 63.2 μmol over 4 h, representing a 33% increase compared to pristine TJU-27-Ru (Fig. S32).

Charge transfer dynamics

Given the excellent photocatalytic performance of TJU-27-Ru for CO_2 reduction, we investigated the photogenerated carrier dynamics using a combination of experimental photophysical studies and DFT calculations. First, a variety of spectroscopic techniques were used to investigate the exciton formation and dissociation processes. Steady-state photoluminescence (PL) spectroscopy revealed that the PL maxima of TJU-27-Ru locating at 630 nm upon 370 nm excitation, which exhibited a substantially lower intensity than that of the pristine $[Ru(H_2dcbpy)_3]\cdot Cl_2$ (Fig. 4a). This suggests that the intercalation of $Ru(bpy)_3$-based ligands into the layered lead halide framework suppresses radiative electron-hole recombination of $Ru(bpy)_3$ complex and provides additional pathways for photogenerated carrier migration. This was further supported by the time-resolved PL spectroscopy of TJU-27-Ru and $[Ru(H_2dcbpy)_3]\cdot Cl_2$ (Fig. 4b). The best fits to tri-exponential function indicated that the PL decay lifetime of TJU-27-Ru (85 ns) was significantly longer than that of $[Ru(H_2dcbpy)_3]\cdot Cl_2$ (34 ns) at room temperature. The decreased PL emission intensity and extended PL lifetime strongly support the photoinduced LMCT process, where the photogenerated electrons are transferred from $Ru(bpy)_3$ photosensitive moieties to the lead halide layers. Indeed, this claim was further corroborated by DOS calculations, which showed that the $Ru(bpy)_3$-based ligand contributes to the VBM and Pb 6*p* orbitals dominate the CBM. Overall, steady-state and transient PL spectroscopy, combined with DOS calculations, confirm that the presence of photoinduced charge transfer from $Ru(bpy)_3$ to lead halide layers suppresses carrier recombination and promotes the electron-hole separation for enhanced photocatalysis.

To gain deeper insight into the dynamics of photocarriers between different excited states, ultrafast transient absorption (TA) spectroscopy was performed using a 420 nm pump laser to probe the real-time carrier behavior of TJU-27-Ru. The pseudo-color TA plot revealed a broad positive photoinduced absorption (PIA) band ranging from 600 nm to 800 nm (Fig. 4c). The contour map shows characteristic TA spectra at various probe delays, where the intensity of the broad positive signal decreases with increasing probe delay time (5 to 1000 ps). This reduction in intensity corresponds to the rapid absorption of photogenerated electrons and holes within the

https://doi.org/10.1038/s41467-025-60954-4

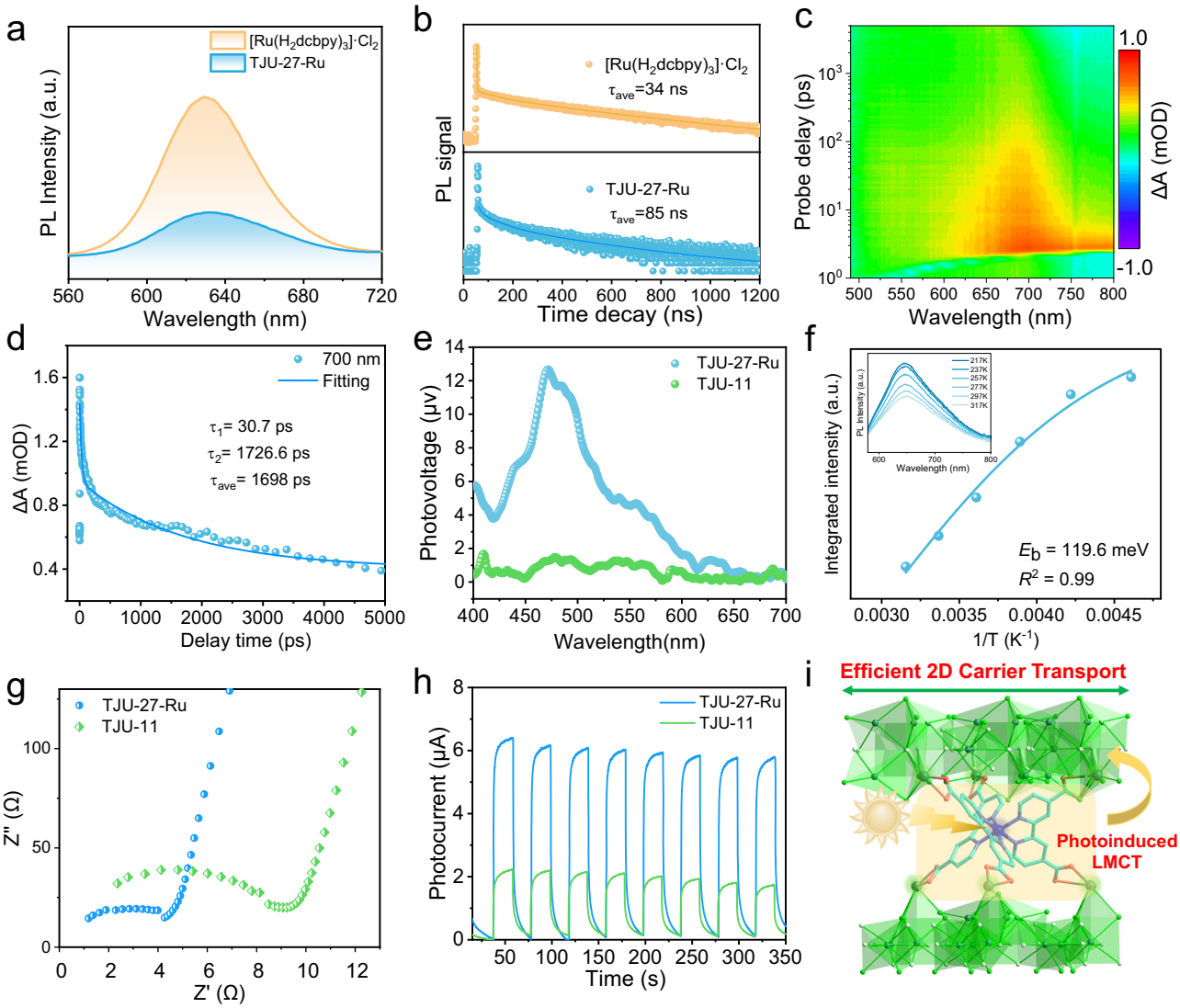

Fig. 4 | Photophysical properties of TJU-27-Ru, $[Ru(H_2dcbpy)_3]\cdot Cl_2$ and TJU-11. **a** PL spectra of TJU-27-Ru and $[Ru(H_2dcbpy)_3]\cdot Cl_2$. **b** PL decay curves and fitting plots of TJU-27-Ru and $[Ru(H_2dcbpy)_3]\cdot Cl_2$. **c** Two-dimensional pseudo-color TA plot of TJU-27-Ru. **d** TA kinetic of TJU-27-Ru. **e** SPV spectra of TJU-27-Ru and TJU-11. **f** Integrated PL emission intensity of TJU-27-Ru as a function of temperature fitted by the Arrhenius equation. Inset: temperature-dependent PL spectra of TJU-27-Ru. **g** EIS Nyquist plots of TJU-27-Ru and TJU-11. **h** Photocurrent responses of TJU-27-Ru and TJU-11. **i** Schematic presentation showing the LMCT process of TJU-27-Ru based on the Pb^{2+}-carboxylate coordination motif. Source data are provided as a Source Data file.

photocatalyst (Fig. S33). In addition, the curve exhibits an ultrafast increase in ΔA, indicating the transient generation of photogenerated charge carriers between 2 ps and 5 ps. A biexponential function was used to fitted to the kinetic decay curve at 700 nm, affording $\tau_1 = 30.7$ ps and $\tau_2 = 1726.6$ ps (Fig. 4d). The fast decay (τ_1) at 30.7 ps is attributed to the recombination of photogenerated carriers and the relaxation of charge carriers at different trap energy levels, while the slower decay(τ_2) at 1726.6 ps is associated with the recombination of trapped carriers during their migration. To further explore photo-induced electron-hole separation and carrier transport behaviors, surface photovoltage (SPV) spectroscopy was employed for both TJU-27-Ru and TJU-11. Both materials exhibited positive photovoltage response signals in the 420 ~ 600 nm range, confirming their *n*-type semiconductor nature (Fig. 4e). Notably, TJU-27-Ru displayed a stronger SPV response than TJU-11, indicating that more photo-generated holes migrate to the surface of TJU-27-Ru and again confirming the superior carrier migration behavior of TJU-27-Ru.

Given that the intercalation of $Ru(bpy)_3$-based moieties significantly inhibits electron-hole recombination, we aimed to investigate their exciton binding energies (E_b) by fitting the variable-temperature PL intensities to the Arrhenius equation, a widely studied method to determine exciton dissociation behavior[63,64]. Variable-temperature PL studies were conducted from 217 to 317 K, and the PL intensities were fitted against temperature to determine E_b using the Eq. 1:

$$I(T) = \frac{I_0}{1 + Ae^{-E_b/k_BT}} \quad (1)$$

where I_0 represents the PL intensity at 0 K, k_B is the Boltzmann constant, A is the proportional constant, and T is the temperature. Both TJU-11 and TJU-27-Ru exhibited thermal quenching, primarily due to thermally activated non-radiative recombination processes (Fig. 4f and Fig. S34). The calculated E_b values for TJU-27-Ru were 119.6 meV and 202.9 meV for TJU-11, respectively. These results suggest that TJU-27-Ru has a higher tendency for exciton dissociation into free carriers compared to TJU-11, indicating that excitons in TJU-27-Ru more readily dissociate into free charges. Moreover, electrochemical impedance

https://doi.org/10.1038/s41467-025-60954-4

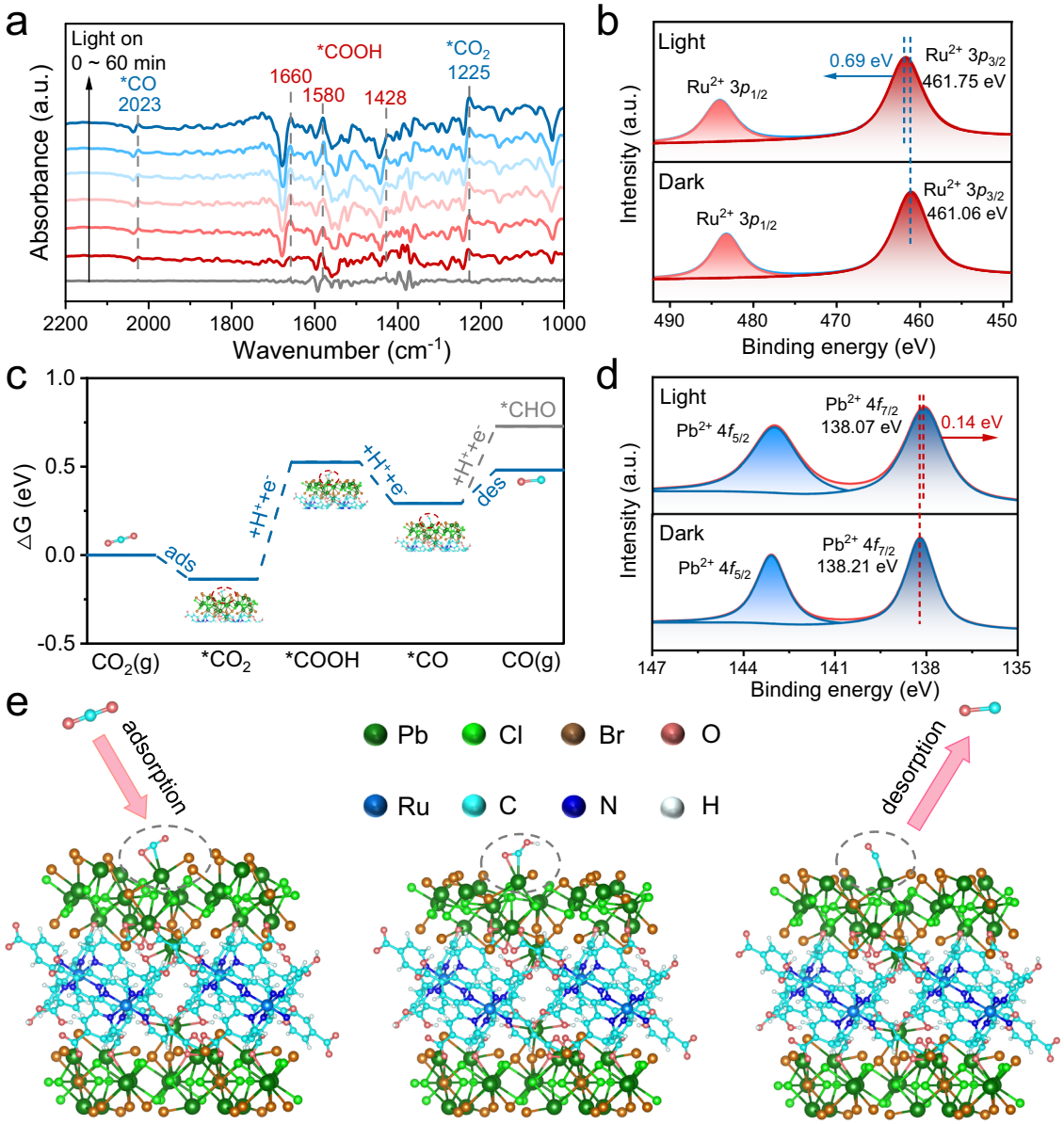

Fig. 5 | In situ DRIFTS measurement, high-resolution XPS spectra and Gibbs free energy calculations. a In situ DRIFTS spectra of TJU-27-Ru during photocatalytic CO_2 reduction. In situ high-resolution XPS spectra under light and dark (light: under visible light (λ > 400 nm) illumination) of Ru 3*p* (**b**), and Pb 4*f* (**d**) for TJU-27-Ru photocatalyst. **c** Calculated free energy (ΔG) diagram of TJU-27-Ru for CO_2 photoreduction to CO. **e** Schematic representation of CO_2 photoreduction mechanism occurring on TJU-27-Ru. Source data are provided as a Source Data file.

spectra (EIS) further confirmed that TJU-27-Ru exhibited a smaller Nyquist semicircle radius compared to TJU-11, indicating lower charge transfer resistance (Fig. 4g). Transient photocurrent testing under illumination with a 300 W Xenon lamp demonstrated obvious photocurrent signals for both TJU-11 and TJU-27-Ru (Fig. 4h). The transient photocurrent intensity of TJU-27-Ru was more than three times higher than that of TJU-11, aligning with our previous observations that TJU-27-Ru generates more free carriers and exhibits enhanced charge separation. Based on these findings, we conclude that the covalent intercalation of photoactive $Ru(bpy)_3$-based pillars into the layered lead halide promotes exciton dissociation into free charges, facilitating charge accumulation on the surface of TJU-27-Ru that enhances the catalytic efficiency of CO_2 photoreduction.

Photocatalytic mechanism

Quasi in situ high-resolution XPS spectra were measured under light and dark conditions to clarify the electron transfer and identify photocatalytic reaction sites. Under visible-light irradiation, XPS measurements revealed a blue-shift in the Ru $3p_{3/2}$ peak of TJU-27- Ru to a higher binding energy by ~0.69 eV compared to the dark condition, indicating a decrease in electron density around the Ru^{2+} centers (Fig. 5b). Meanwhile, the Pb $4f_{7/2}$ peak shifted to a lower binding energy by ~0.14 eV, suggesting an increase in electron density at the Pb^{2+} sites upon photoexcitation (Fig. 5d). These change in electron density are consistent with our previous findings on carrier dynamics, supporting photoexcited charge transfer process from the $Ru(bpy)_3$ intercalates to the lead halide layers. The electron-enriched Pb^{2+} sites facilitate CO_2 adsorption and activation, contributing to the photocatalytic process.

To dynamically monitor intermediate species during the photocatalytic process, in situ diffuse reflectance infrared Fourier transform spectroscopy (in situ DRIFTS) were conducted on TJU-27-Ru under photocatalysis conditions (Fig. 5a). The active $*CO_2$ species observed near 1225 cm^{-1} indicates that the initial step of photocatalytic CO_2 reduction involves CO_2 binding to the catalyst. This observation is

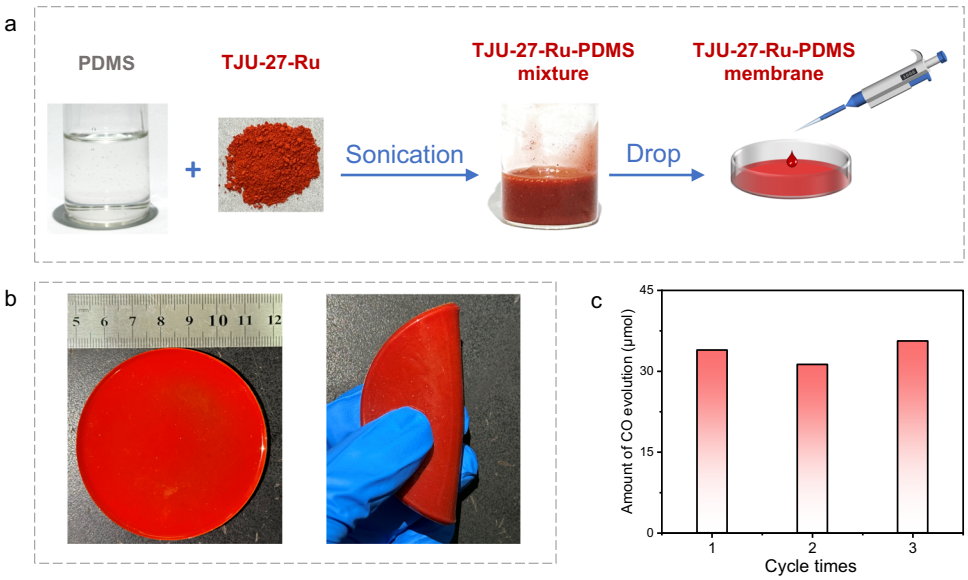

Fig. 6 | Synthetic scheme and CO_2 photoreduction performance of TJU-27-Ru-PDMS membrane. a Schematic illustration for the fabrication of TJU-27-Ru-PDMS membrane by a simple drop casting method. **b** The digital photographs of the as-prepared TJU-27-Ru-PDMS membrane, the membrane is free-standing, flexible, as shown by the photos on the right. **c** Photocatalytic CO_2 reduction of TJU-27-Ru-PDMS membrane in 3 h in 5 mL MeCN with 0.1 M BIH. Source data are provided as a Source Data file.

consistent with our Gibbs free energy calculations, which provide insights into the CO_2 photoreduction mechanism (Fig. 5c). These calculations show that CO_2 is initially activated by Pb^{2+} sites, forming the intermediate $*CO_2$ with a reduced Gibbs free energy and suggesting the thermodynamically favorable process for CO_2 adsorption and activation on TJU-27-Ru. With prolonged irradiation, bands at 1660, 1580, and 1428 cm^{-1} become more intense in the DRIFTS spectra, suggesting the formation of *COOH species that is an essential intermediate in the CO_2 photoreduction process. This step involves protonation at one of the oxygens for $*CO_2$, identified as the rate-determining step by DFT calculations. TJU-27 exhibits a relatively low energy barrier of 0.66 eV for this step, lower than those of many previously reported metal halide photocatalysts[24,46]. This reduction in energy barrier probably results from the asymmetric coordination of external lead atoms instead of symmetric $[PbX_6]$ octahedra as for perovskites, which have coordination sites to form a more stable binding configuration with the *COOH intermediate. In addition, a peak at 2038 cm^{-1}, corresponding to the *CO intermediate, is associated with the formation of the final CO product. The free energy profile for protonating *COOH to *CO reveals a downhill process, indicating the spontaneous transformation on the Pb^{2+} sites followed by the energetically favorable release of CO.

To further study the origin of high CO selectivity for TJU-27-Ru, Gibbs free energy calculations were performed for the hydrogenation of *CO intermediate. The calculated energy for *CHO (ΔG(*CHO)) is higher than the desorption energy of CO, owing to the weakly bonded *CO intermediate (Fig. S35). This implies that TJU-27-Ru more readily facilitates *CO desorption than the protonation of *CO to produce *CHO, explaining its near-quantitative selectivity for visible-light-driven CO_2 reduction to CO. Therefore, the most probable pathway for the photocatalytic CO_2 reduction is summarized as follows:

$$CO_2(g) \rightarrow *CO_2 \quad (2)$$

$$*CO_2 + e^- + H^+ \rightarrow *COOH \quad (3)$$

$$*COOH + e^- + H^+ \rightarrow *CO + H_2O \quad (4)$$

$$*CO \rightarrow CO\uparrow \quad (5)$$

Based on these findings, we propose a plausible reaction mechanism for the photocatalytic CO_2 reduction on TJU-27-Ru. Upon visible light irradiation, interlamellar $[Ru(Hdcbpy)_3^-]$ moieties are first excited to the $[Ru(Hdcbpy)_3^-]^*$ state, facilitating the transfer of photoinduced electrons to the Pb^{2+} centers. Subsequently, CO_2 adsorbed on the lead halide surface undergoes partial reduction and hydrogenation to produce *COOH intermediates, which are further converted to CO. The oxidized $[Ru(Hdcbpy)_3^-]$ in TJU-27-Ru is regenerated by the sacrificial electron donor, thereby completing the photocatalytic cycle.

Given the high demands for catalyst separation in practical CO_2 photoreduction, we developed a proof-of-concept photocatalyst membrane using TJU-27-Ru and poly(dimethylsiloxane) (PDMS) as a polymer binding (Fig. 6a). The resultant flexible, robust and free-standing membrane was fabricated by simple drop-casting of the suspension (Fig. 6b). The thickness of the TJU-27-Ru membrane was measured to be 0.59 mm using a vernier caliper (Fig. S36). The TJU-27-Ru membrane demonstrates efficient photocatalytic CO_2 reduction with high stability and reusability, achieving an average CO evolution of 33.6 μmol over three consecutive cycles (Fig. 6c). Unlike homogeneous $[Ru(bpy)_3]^{2+}$ complexes or $CsPbBr_3$ quantum dots, the TJU-27-Ru membrane can be easily separated from the reaction solution, allowing for straightforward preparation for repeated photocatalysis runs. The slight decrease in photocatalytic performance compared to microscopic TJU-27-Ru powders is probably due to the formation of a compact layer, which limits the exposure of active catalyst surfaces for photocatalysis reactions. Nevertheless, TJU-27-Ru membrane demonstrated stable CO production for 26 μmol CO in 3 h under natural sunlight, while no product was detected in the absence of light or under an argon environment (Fig. S37). This demonstration confirms the applicability of our $Ru(bpy)_3$-intercalated layered lead halide framework for practical photocatalysis applications.

Discussion

In summary, we have synthesized a layered lead halide material intercalated with $[Ru(bpy)_3]^{2+}$ complexes through Pb^{2+}-carboxylate bonding, achieving both enhanced photophysical properties and high chemical stability. The intercalation of $[Ru(bpy)_3]^{2+}$ ligands modulates the electronic structure near the valence band, extending the absorption edge to 680 nm. This layered compound enables efficient

photoinduced charge transfer from $[Ru(bpy)_3]^{2+}$ centers to the lead halide layers and suppresses radiative electron-hole recombination of the $[Ru(bpy)_3]^{2+}$ complexes. The efficient visible-light absorption of $[Ru(bpy)_3]^{2+}$ centers and the excellent carrier transport of lead halide layers synergistically achieve efficient photocatalytic CO_2 reduction, affording an impressive AQE of ~3.0% at 500 nm. This performance surpasses all of previously reported single-component hybrid lead halides, as well as heterojunction constructions based on hybrid lead halides.

Importantly, TJU-27-Ru demonstrates efficient CO_2-to-CO photoreduction performances even under natural sunlight and can be fabricated into flexible, robust and free-standing membranes for practical applications in artificial photosynthesis. Mechanistic insights from in situ DRIFTS measurements and theoretical calculations reveal that the intercalation of $[Ru(bpy)_3]^{2+}$ ligands facilitates photoinduced charge transport, thereby enhancing CO_2 adsorption and activation. This process effectively lowers the reaction energy barrier for the formation of the key *COOH intermediate during CO_2-to-CO photoreduction. This work introduces a coordination-driven intercalation strategy for constructing robust layered lead halide frameworks, paving the way for further advancements in metal halide photocatalysts.

Methods

Materials

All starting reagents, materials, and solvents were purchased froma commercial supplier and used without further purification. Rutheniu-m(III) trichloride trihydrate ($RuCl_3{\cdot}3H_2O$, 98%+, Adamas), 2,2′-bipyridine-4,4′-dicarboxylic acid ($C_{12}H_8N_2O_4$, H_2dcbpy, 98%+, Adamas), lead bromide ($PbBr_2$, 99%, Aladdin), trans-1,4-cyclohexanedicarboxylic acid (trans-1,4-chdc, >98%, Adamas-beta), 1,4-diaminobutane ($C_4H_{12}N_2$, 98% +, Adamas), perchloric acid (70% in H_2O, SCR), hydrobroic acid (48% in water), acetonitrile (CH_3CN, >99%, Greagent), ethanol (EtOH, >99.5%, Greagent), deionized water was obtained from a Barnstead Pacific RO water purification system.

Synthesis of $[Ru(H_2dcbpy)_3]{\cdot}Cl_2$

$[Ru(H_2dcbpy)_3]{\cdot}Cl_2$ was synthesized by following the published procedure[39]. $RuCl_3{\cdot}3H_2O$ (50 mg) and H_2dcbpy (140 mg) were placed in a 23 mL Teflon-lined stainless container where 1 mL of HCl (37%) and 2 mL of water were added. The mixture was heated at 200 °C for 4 h and cooled to room temperature. The dark red block crystals were filtered off and washed thoroughly with water. Yield: 152 mg (83%).

Synthesis of TJU-27-Ru

$PbBr_2$ (59 mg, 0.16 mmol), $[Ru(H_2dcbpy)_3]{\cdot}Cl_2$ (72 mg, 0.08 mmol) and 8 mL solvents of MeCN/H_2O (2:1 v:v) were added into a 15 mL Teflon-lined autoclave, followed by 15 min stirring for sufficient dispersion. The autoclave was then sealed and heated statically at 110 °C for 72 h. Upon the autoclave cooling to room temperature, the red platelike crystals were isolated by vacuum filtration, rinsed with ethanol, and then dried at 60 °C under air for 10 h (yield: 46 mg, ~59% based on Pb). Element analysis: calculated C, 15.75%; H, 0.77%; N, 3.06%; found C, 16.05%; H, 0.72%; N, 3.10%.

Synthesis of TJU-11

The material was synthesized according to the previous report[20]. ~0.544 g $PbBr_2$ (1.5 mmol), 0.16 g trans-1,4-chdcNa_2 (0.75 mmol) and hydrobromic acid (50 µL) were dispersed in 8 mL deionized water using sonication. Then the mixture was transferred to a 15 mL Teflon-lined autoclave reactor, which was statically heated at 150 °C for 3 days. Then the autoclave was cooled to room temperature, and colorless block-shaped crystals of TJU-11 were isolated by vacuum filtration. The crystals were rinsed with ethanol three times (3 × 10 mL), and dried under air (yield: 400 mg, ~71% based on Pb).

Synthesis of $(C_4H_{14}N_2)[PbBr_4]$ Perovskite

The material was synthesized according to the previous report[62]. ~0.099 g $PbBr_2$ (0.270 mmol) was dissolved in 3 ml 48% HBr in a sample vial. Thereafter, 0.022 g $NH_2C_4H_8NH_2$ (0.250 mmol) was added, and the precipitate dissolved by refluxing at 85 °C. The solution was slowly cooled at 2 °C h^{-1} to room temperature. The colorless single crystals were filtered out and dried under air (yield: 85 mg, ~51% based on Pb).

Photodeposition of Rh Co-catalyst

Rh nanoparticles were photodeposited onto the as-synthesized photocatalysts by using $RhCl_3{\cdot}3H_2O$ as the metal precursor. Specifically, 30 mg of photocatalysts in the form of microcrystalline powders were first dispersed in a mixed solution of 1.5 mL H_2O and 1.5 mL methanol containing 0.76 mg $RhCl_3{\cdot}3H_2O$ (2.9 µmol) (Table S4). The mixture was then irradiated by a Xe lamp for 60 min. After that, the solids were isolated by centrifugation, washed with water and ethanol for three times, and dried at 60 °C in ambient condition for 24 h.

Preparation of TJU-27-Ru Membrane

First, as-synthesized TJU-27-Ru crystals (50 mg) were manually grounded to fine powder using an agate mortar, and poly(-dimethylsiloxane) (PDMS) (5.5 g) was prepared by mixing the pre-polymer with a curing agent in the volume ratio of 10:1. Then, the resultant TJU-27-Ru powder were mixed with PDMS. The obtained colloidal solution was under continuous ultrasonication for ~50 min and drop-casted on an evaporating dish to prepare a membrane, followed by heating at 70 °C under vacuum to remove the air bubbles. The membrane was peeled off from the dish for photocatalysis.

Materials characterization

Optical microscope images of TJU-27-Ru were collected by Nikon ECLPSE LV100NPOL. Powder X-ray diffraction (PXRD) analysis were collected on a Bruker D2 Phaser X-ray diffractometer equipped with a Cu sealed tube (λ = 1.54184 Å). The diffraction patterns were scanned at 30 kV and 10 mA with a scan speed of 1 s per step, a step size of 0.02° in 2θ, and a 2θ range of 5-40°. Fourier transform infrared spectroscopy were collected using a BRUKER ALPHA spectrophotometer with a wavenumber region of 4000–400 cm^{-1}. Elemental analysis (EA) for C/H/N were performed in a Varian EL III element analyzer. Thermogravimetry analysis (TGA) were carried out on a TGA Q5000 differential thermal analyzer. The TJU-27-Ru samples were heated in a N_2 stream from room temperature to 800 °C with a heating rate of 10 °C/min. Ultraviolet−visible (UV−vis) diffuser reflectance spectroscopy was performed on a Shimadzu UV-2600 ultraviolet−visible spectrophotometer equipped with an integrating sphere, using 100% $BaSO_4$ as the reflectance standard for all measurements. UV photoelectron spectra (UPS) were collected by a Shimadu/Kratos Axis Supra spectrometer with He I radiation (21.22 eV). Valence band X-ray photoelectron spectroscopy were carried out on a JEOL AXIS-ULTRA DLD. The emission spectra of TJU-27-Ru was measured on a HORIBA FLUOROLOG-3 setup in reflection geometry. Time-resolved photoluminescence were performed at room temperature with a time-correlated single photon counting (TCSPC) technique on HORIBA FLUOROLOG-3. The excitation wavelength was 370 nm provided by an EPL-360PS pulsed diode laser. The lifetimes were calculated by fitting data to an exponential decay function using fluorescence decay analysis software. Temperature-dependent emission of TJU-27-Ru was carried out on Edinburgh FLS1000 equipped with autotuning temperature controller, where the temperature of the sample chamber was gradually changed from 217 K to 317 K. Surface photovoltaic (SPV) spectra were performed on the basis of a lock-in amplifier (Sr830-D SP). The measurement systems include a computer, a light chopper (SR540), monochromatic light, and a sample cell. X-ray photoelectron spectroscopy (XPS) was performed on an EscaLab 250i X-ray photoelectron spectrometer (ThermoFisher,

USA) equipped with an Al Kα excitation source. In situ irradiated XPS was performed with external light source irradiation (300 W Xe lamp, Beijing Perfectlight Technology Co., Ltd., China) on the basis of XPS measurements. Nuclear magnetic resonance (NMR) spectra were carried out on an Advance III HD spectrometer (600 MHz); chemical shifts were quoted in parts per million (ppm) referenced to the appropriate solvent peak or 0 ppm for tetramethylsilane (TMS).

Single-crystal X-ray crystallography (SCXRD)

First, high-quality single crystals of $[Ru(H_2dcbpy)_3]\cdot Cl_2$ and TJU-27-Ru were selected under an optical microscope (NIKON ECLIPSE LV100N POL) and mounted on glass fibers. Single crystal X-ray diffraction data for $[Ru(H_2dcbpy)_3]\cdot Cl_2$ and TJU-27-Ru were obtained using a Bruker D8 Venture diffractometer equipped with a Photon III detector. Table S1 and Table S2 summarize the crystal data and details of the structural refinement. The diffraction data were subsequently processed using the APEX3 software package: integrated using the SAINT program and corrected for empirical absorption using SADABS. The determination of the space group was based on systematic extinction, E statistics, the consistency factor of equivalent reflections, and the successful results of structural refinement. The structural solution was achieved using the direct method, followed by conventional Fourier expansion, and all reflections were refined using the SHELXTL software package based on F^2 via full-matrix least-squares refinement. All non-hydrogen atoms were modeled using anisotropic displacement parameters. Hydrogen atoms were constrained to carrier atoms using the same isotropic displacement parameters as the bonded atoms.

Chemical and thermal stability

~200 mg of the as-synthesized materials were incubated in pure water and organic solvents (including EtOH, MeOH, acetone, and i-PrOH), respectively. The samples were incubated into the above conditions for 24 h before performing PXRD measurements. Thermal stability was conducted by heating the as-synthesized crystals in an oven at 100 °C, 150 °C, and 200 °C for 24 h in air, followed by PXRD characterization after cooling to room temperature.

Photocatalytic CO_2 reduction

The photocatalytic CO_2 reduction tests were carried out in a quartz reaction vessel with sealing components. Typically, 30 mg of photocatalyst and 5 mL reaction solution (5 mL H_2O or 0.1 M BIH in 5 mL MeCN) with sonication for 15 min to get a uniformly dispersed suspension. Then, the mixture was purged with high purity CO_2 for 20 min to remove air, ensuring that the final reactor was filled with CO_2. Subsequently, the suspension was irradiated under a 300 W Xe lamp (PLS-SXE300/300UV, Beijing Perfect Light Technology Co., Ltd.). The wavelength range of the Xe lamp is 320–780 nm, and the standard sun unit for the AM1.5 G simulator is 277 mW/cm^2. The mixture was kept stirring during photocatalytic reaction. The temperature of the reaction cell was set at 5 °C by recirculating cooling water system during irradiation. The gaseous products were measured by an online gas chromatograph (GC9790 II(MC-02), Fuli Analytical Instrument Co., Ltd.) with a thermal conductivity detector (TCD) for H_2 and O_2 determination, and a flame ionization detector (FID) for CO and CH_4 determinations. The liquid product was characterized by ^{1}H NMR spectroscopy. The multiple-run study was performed by using 30 mg of photocatalyst, and the system was evacuated and refilled CO_2 for every 4 h. The standard sun unit for natural sunlight is approximately 80–120 mW/cm^2.

Apparent Quantum Efficiencies (AQEs) Measurement

The AQEs for the conversion of CO_2 to CO were measured on the same photocatalytic setup, except that 300 W Xe lamp was covered with a band-pass filter to simulate specific wavelengths (λ = 500, 550, 600, 650, 700 nm). The number of incident photons was measured by a radiant power energy meter (PL-MW2000 Light Radiometer, Perfect Lighting Co., Ltd.). The AQEs of CO_2 to CO conversion is calculated as follows:

$$\begin{aligned} AQE(\%) &= \frac{number\ of\ reacted\ photogenerated\ electrons}{number\ of\ incident\ photons} \\ &= \frac{2\times number\ of\ produced\ CO}{number\ of\ incident\ photons} = \frac{2\times N_A\times n}{N_{photon}} \end{aligned} \tag{6}$$

$$N_{photon} = \frac{A\times I\times t\times \lambda}{h\times c} \tag{7}$$

where N_A is Avogadro's constant, n is the molar amount of produced CO, A is the irradiated area of reaction system, I is the light intensity, t is the reaction time, λ is the wavelength of light, h is Planck's constant, and c is the speed of light.

Electrochemical measurement

The photocurrent responses and electrochemical impedance spectroscopy measurements were carried out on a CHI 760E electrochemical workstation (Shanghai Chenhua) equipped with a standard three-electrode system, including an indium-tin oxide (ITO) deposited with samples as the working electrode, an Ag/AgCl (KCl saturated) reference electrode and a Pt counter electrode. A 0.5 M Na_2SO_4 aqueous solution was used as the electrolyte. The working electrodes were prepared as follows: 10 mg of the photocatalyst samples were dispersed in a mixed solution of H_2O (1 mL), methanol (1 mL) and Nafion (10 μL) by sonication, and 100 μL of the above mixtures was coated on one side of ITO electrode followed by drying at room temperature. The frequency range was measured from 1 Hz to 1 MHz. In the photocurrent measurements, a 300 W Xenon lamp with the AM 1.5 G filter was served as the incident light.

In situ DRIFTS

In situ DRIFTS was performed on a Thermo Scientific Nicolet 6700FT spectrometer. First, the reaction solution and photocatalyst were placed separately at the bottom of the sample cell. After vacuum degassing for 30 min, the background spectra were collected. Followed by this, a mixture of CO_2 and reaction solution vapor were introduced into the sample cell. A 300 W Xenon lamp was employed to irradiate the sample cell through a quartz window and the spectra were collected at 5 min intervals.

Computational details

The band structure and PDOS of TJU-33 is calculated by density functional theory method implemented in the Vienna Ab initio Simulation Package (VASP) code[65,66]. The generalized gradient approximation (GGA) of Perdew-Burke-Ernzerhof (PBE) was used to describe the exchange-correlation functional[67]. The cut-off energy for the plane wave basis was set to 450 eV and a 4 × 4 × 2 Monkhorst-pack mesh was employed. The calculation converges the total energy to be lower than 1.0×10^{-4} eV per atom. The Hellmann-Feynman force on each atom was converged to lower than 0.02 eV/Å.

The computational hydrogen electrode model developed by Nørskov et al.[68] has been adopted for calculations of the Gibbs free-energy change (ΔG) for the reaction elemental step and the reaction-free energies can be described as[69]:

$$\Delta G = \Delta E + \Delta E_{ZPE} - T\Delta S \tag{8}$$

where E, E_{ZPE} and S were the total energy, the zero-point energy, entropy and the number of electrons involved in the reaction.

Data availability

The data supporting the findings of this study are available in the paper and Supplementary Information files. The X-ray crystallographic coordinates for structures reported in this study have been deposited at the

Cambridge Crystallographic Data Centre (CCDC), under deposition number 2402625 (TJU-27-Ru) and 2402491 ([Ru(H_2dcbpy)$_3$]·Cl_2). The data can be obtained free of charge from The Cambridge Crystallographic Data Centre via www.ccdc.cam.ac.uk/data_request/cif. Source data are provided as a Source Data file. All data in the article and supplementary information are available from the corresponding authors upon request. Source data are provided with this paper.

References

1. Chouhan, L., Ghimire, S., Subrahmanyam, C., Miyasaka, T. & Biju, V. Synthesis, optoelectronic properties and applications of halide perovskites. *Chem. Soc. Rev.* **49**, 2869–2885 (2020).
2. Kazim, S., Nazeeruddin, M. K., Grätzel, M. & Ahmad, S. Perovskite as Light Harvester: A game changer in photovoltaics. *Angew. Chem. Int. Ed.* **53**, 2812–2824 (2014).
3. Huang, H. et al. Metal halide perovskite based heterojunction photocatalysts. *Angew. Chem. Int. Ed.* **61**, e202203261 (2022).
4. Stranks, S. D. & Snaith, H. J. Metal-halide perovskites for photovoltaic and light-emitting devices. *Nat. Nanotechnol.* **10**, 391–402 (2015).
5. D'Innocenzo, V. et al. Excitons versus free charges in organo-lead tri-halide perovskites. *Nat. Commun.* **5**, 3586 (2014).
6. Snaith, H. J. Perovskites: The emergence of a new era for low-cost, high-efficiency solar cells. *J. Phys. Chem. Lett.* **4**, 3623–3630 (2013).
7. Wang, R. et al. A review of perovskites solar cell stability. *Adv. Funct. Mater.* **29**, 1808843 (2019).
8. Christians, J. A., Miranda Herrera, P. A. & Kamat, P. V. Transformation of the excited state and photovoltaic efficiency of ch3nh3pbi3 perovskite upon controlled exposure to humidified air. *J. Am. Chem. Soc.* **137**, 1530–1538 (2015).
9. Leung, T. L. et al. Stability of 2D and quasi-2D perovskite materials and devices. *Commun. Mater.* **3**, 63 (2022).
10. Zheng, H. et al. The effect of hydrophobicity of ammonium salts on stability of quasi-2d perovskite materials in moist condition. *Adv. Energy Mater.* **8**, 1800051 (2018).
11. Tailor, N. K. et al. The effect of dimensionality on the charge carrier mobility of halide perovskites. *J. Mater. Chem. A* **9**, 21551–21575 (2021).
12. Hoye, R. L. Z. et al. The role of dimensionality on the optoelectronic properties of oxide and halide perovskites, and their halide derivatives. *Adv. Energy Mater.* **12**, 2100499 (2022).
13. He, T., Jiang, Y., Xing, X. & Yuan, M. Structured perovskite light absorbers for efficient and stable photovoltaics. *Adv. Mater.* **32**, 1903937 (2020).
14. Zhang, H. et al. Metal Sulfide S-scheme homojunction for photocatalytic selective phenylcarbinol oxidation. *Adv. Sci.* **11**, 2400099 (2024).
15. Huang, H. et al. Noble-metal-free high-entropy alloy nanoparticles for efficient solar-driven photocatalytic CO_2 reduction. *Adv. Mater.* **36**, 2313209 (2024).
16. Zhang, Z.-X. et al. Organometallic-based hybrid perovskite piezoelectrics with a narrow band gap. *J. Am. Chem. Soc.* **142**, 17787–17794 (2020).
17. Sun, C., Xi, R. & Fei, H. Organolead halide-based coordination polymers: intrinsic stability and photophysical applications. *Acc. Chem. Res.* **56**, 452–461 (2023).
18. Jiang, Y., Yin, J. & Fei, H. Lowering the dimensionality of cationic lead bromide units in robust coordination polymers for enhanced self-trapped broadband emission. *J. Mater. Chem. C.* **10**, 13254–13261 (2022).
19. Song, X. et al. Overall photocatalytic water splitting by an organo-lead iodide crystalline material. *Nat. Catal.* **3**, 1027–1033 (2020).
20. Yin, J., Yang, H. & Fei, H. Robust, cationic lead halide layered materials with efficient broadband white-light emission. *Chem. Mater.* **31**, 3909–3916 (2019).
21. Yang, H., Yin, J., Xu, X. & Fei, H. Enhanced intrinsic white-light emission upon near-UV excitation by crystal engineering of cationic lead bromide layered materials. *J. Mater. Chem. C.* **7**, 7090–7095 (2019).
22. Zhuang, Z. et al. Intrinsic broadband white-light emission from ultrastable, cationic lead halide layered materials. *Angew. Chem. Int. Ed.* **56**, 14411–14416 (2017).
23. Yin, J. et al. Modulating inorganic dimensionality of ultrastable lead halide coordination polymers for photocatalytic CO2 reduction to ethanol. *Angew. Chem. Int. Ed.* **63**, e202316080 (2024).
24. Chen, X. et al. Bromo- and iodo-bridged building units in metal-organic frameworks for enhanced carrier transport and CO_2 photoreduction by water vapor. *Nat. Commun.* **13**, 4592 (2022).
25. Stoumpos, C. C. et al. Ruddlesden-popper hybrid lead iodide perovskite 2D homologous semiconductors. *Chem. Mater.* **28**, 2852–2867 (2016).
26. De Armond, M. K. & Myrick, M. L. The life and times of $[Ru(bpy)_3]^{2+}$: localized orbitals and other strange occurrences. *Acc. Chem. Res.* **22**, 364–370 (1989).
27. Nakajima, T. et al. Photocatalytic reduction of low concentration of CO_2. *J. Am. Chem. Soc.* **138**, 13818–13821 (2016).
28. Pettersson Rimgard, B. et al. Ultrafast interligand electron transfer in cis-$[Ru(4,4'$-dicarboxylate-$2,2'$-bipyridine$)_2(NCS)_2]^{4-}$ and implications for electron injection limitations in dye sensitized solar cells. *Chem. Sci.* **9**, 7958–7967 (2018).
29. Limburg, B., Bouwman, E. & Bonnet, S. Rate and stability of photocatalytic water oxidation using $[Ru(bpy)_3]^{2+}$ as photosensitizer. *ACS Catal.* **6**, 5273–5284 (2016).
30. Gao, F. G. & Bard, A. J. Solid-state organic light-emitting diodes based on tris(2,2′-bipyridine)ruthenium(II) complexes. *J. Am. Chem. Soc.* **122**, 7426–7427 (2000).
31. Lin, X. et al. Photocatalytic CO_2 reduction promoted by uniform perovskite hydroxide $CoSn(OH)_6$ nanocubes. *Appl. Catal. B: Environ.* **224**, 1009–1016 (2018).
32. Himiyama, T. et al. A heterogeneous hydrogen-evolution catalyst based on a mesoporous organosilica with a diiron catalytic center modelling [FeFe]-hydrogenase. *ChemCatChem* **10**, 4894–4899 (2018).
33. Gao, Y. et al. Perovskite hydroxide $CoSn(OH)_6$ nanocubes for efficient photoreduction of CO_2 to CO. *ACS Sustain. Chem. Eng.* **6**, 781–786 (2018).
34. Hong, D., Yamada, Y., Nagatomi, T., Takai, Y. & Fukuzumi, S. Catalysis of nickel ferrite for photocatalytic water oxidation using $[Ru(bpy)_3]^{2+}$ and $S_2O_8^{2-}$. *J. Am. Chem. Soc.* **134**, 19572–19575 (2012).
35. Bossmann, S. H. et al. $Ru(bpy)_3^{2+}/TiO_2$-codoped zeolites: Synthesis, characterization, and the role of TiO_2 in electron transfer photocatalysis. *J. Phys. Chem. B* **105**, 5374–5382 (2001).
36. Kumar, P., Joshi, C., Labhsetwar, N., Boukherroub, R. & Jain, S. L. A novel Ru/TiO_2 hybrid nanocomposite catalyzed photoreduction of CO_2 to methanol under visible light. *Nanoscale* **7**, 15258–15267 (2015).
37. Song, Y. et al. Titanium hydroxide secondary building units in metal-organic frameworks catalyze hydrogen evolution under visible light. *J. Am. Chem. Soc.* **141**, 12219–12223 (2019).
38. Cadiau, A. et al. A titanium metal-organic framework with visible-light-responsive photocatalytic activity. *Angew. Chem. Int. Ed.* **59**, 13468–13472 (2020).
39. Zhang, S. et al. A highly symmetric metal-organic framework based on a propeller-like ru-organic metalloligand for photocatalysis and explosives detection. *Cryst. Growth Des.* **13**, 5466–5472 (2013).
40. Xu, L. et al. Solvent selective effect occurs in iodinated adamantanone ferroelectrics. *Adv. Sci.* **9**, 2201702 (2022).
41. Ge, F., Cheng, P., Li, Q., Xu, J. & Bu, X.-H. Achiral fluorinated aromatic ligands based chiral hybrid antimony halides with high-efficiency second-harmonic generation. *Adv. Optical Mater.* **11**, 2301040 (2023).

42. Hu, J., Yan, L. & You, W. Two-dimensional organic-inorganic hybrid perovskites: a new platform for optoelectronic applications. *Adv. Mater.* **30**, 1802041 (2018).
43. Xiao, Y. et al. Visible-light-responsive 2d cadmium-organic framework single crystals with dual functions of water reduction and oxidation. *Adv. Mater.* **30**, 1803401 (2018).
44. Xu, Y.-F. et al. A $CsPbBr_3$ perovskite quantum dot/graphene oxide composite for photocatalytic CO_2 reduction. *J. Am. Chem. Soc.* **139**, 5660–5663 (2017).
45. Wu, L.-Y. et al. Encapsulating perovskite quantum dots in iron-based metal-organic frameworks (MOFs) for efficient photocatalytic CO_2 reduction. *Angew. Chem. Int. Ed.* **58**, 9491–9495 (2019).
46. Wang, X. et al. Immobilizing perovskite $CsPbBr_3$ nanocrystals on Black phosphorus nanosheets for boosting charge separation and photocatalytic CO_2 reduction. *Appl. Catal. B: Environ.* **277**, 119230 (2020).
47. Mu, Y.-F. et al. Ultrathin and small-size graphene oxide as an electron mediator for perovskite-based Z-scheme system to significantly enhance photocatalytic CO_2 reduction. *Small* **16**, 2002140 (2020).
48. Dong, G.-X. et al. A halide perovskite as a catalyst to simultaneously achieve efficient photocatalytic CO_2 reduction and methanol oxidation. *Chem. Commun.* **56**, 4664–4667 (2020).
49. Que, M. et al. Anchoring of formamidinium lead bromide quantum dots on Ti_3C_2 nanosheets for efficient photocatalytic reduction of CO_2. *ACS Appl. Mater. Interfaces* **13**, 6180–6187 (2021).
50. Li, L., Zhang, Z., Ding, C. & Xu, J. Boosting charge separation and photocatalytic CO_2 reduction of $CsPbBr_3$ perovskite quantum dots by hybridizing with P3HT. *Chem. Eng. J.* **419**, 129543 (2021).
51. Ou, M. et al. Amino-assisted anchoring of $CsPbBr_3$ perovskite quantum dots on porous g-C_3N_4 for enhanced photocatalytic CO_2 reduction. *Angew. Chem. Int. Ed.* **57**, 13570–13574 (2018).
52. Chen, Q., Lan, X., Chen, K., Ren, Q. & Shi, J. Construction of WO_3/$CsPbBr_3$ S-scheme heterojunction via electrostatic self-assembly for efficient and long-period photocatalytic CO_2 reduction. *J. Colloid Interf. Sci.* **616**, 253–260 (2022).
53. Zhang, G. et al. Interfacial engineering of semicoherent interface at purified $CsPbBr_3$ quantum dots/2D-PbSe for optimal CO_2 photoreduction performance. *ACS Appl. Mater. Interfaces* **14**, 44909–44921 (2022).
54. Ding, L. et al. Embedding $Cs_2AgBiBr_6$ QDs into Ce-UiO-66-H to in situ construct a novel bifunctional material for capturing and photocatalytic reduction of CO_2. *Chem. Eng. J.* **446**, 137102 (2022).
55. Wu, D. et al. Synthesis of stable lead-free $Cs_3Sb_2(Br_xI_{1-x})_9$ ($0 \le x \le 1$) perovskite nanoplatelets and their application in CO2 photocatalytic reduction. *Small* **18**, 2106001 (2022).
56. Bhosale, S. S. et al. Mechanism of photocatalytic CO_2 reduction by bismuth-based perovskite nanocrystals at the gas-solid interface. *J. Am. Chem. Soc.* **141**, 20434–20442 (2019).
57. Liu, Y.-W. et al. Mn-doped $CsPb(Br/Cl)_3$ mixed-halide perovskites for CO_2 photoreduction. *Nanotechnology* **31**, 215605 (2020).
58. Kong, Z.-C. et al. Immobilizing $Re(CO)_3Br$(dcbpy) complex on $CsPbBr_3$ nanocrystal for boosted charge separation and photocatalytic CO_2 reduction. *Sol. RRL* **4**, 1900365 (2020).
59. Bera, S., Shyamal, S. & Pradhan, N. chemically spiraling $CsPbBr_3$ perovskite nanorods. *J. Am. Chem. Soc.* **143**, 14895–14906 (2021).
60. Chen, Z. et al. Boosting photocatalytic CO_2 reduction on $CsPbBr_3$ perovskite nanocrystals by immobilizing metal complexes. *Chem. Mater.* **32**, 1517–1525 (2020).
61. Xu, S. et al. Monochromatic light-enhanced photocatalytic CO_2 reduction based on exciton properties of two-dimensional lead halide perovskites. *Dalton Trans.* **51**, 8036–8045 (2022).
62. Lemmerer, A. & Billing, D. G. Lead halide inorganic-organic hybrids incorporating diammonium cations. *CrystEngComm* **14**, 1954–1966 (2012).
63. Fu, G. et al. Construction of thiadiazole-bridged sp^2-carbon-conjugated covalent organic frameworks with diminished excitation binding energy toward superior photocatalysis. *J. Am. Chem. Soc.* **146**, 1318–1325 (2024).
64. Gao, X. et al. Rational regulation of the exciton effect of acrylonitrile-linked covalent organic framework toward boosting visible-light-driven hydrogen evolution. *ACS Catal.* **14**, 533–546 (2024).
65. Kresse, G. & Furthmüller, J. Efficiency of ab-initio total energy calculations for metals and semiconductors using a plane-wave basis set. *Comp. Mater. Sci.* **6**, 15–50 (1996).
66. Kresse, G. & Joubert, D. From ultrasoft pseudopotentials to the projector augmented-wave method. *Phys. Rev. B* **59**, 1758–1775 (1999).
67. Perdew, J. P., Burke, K. & Ernzerhof, M. Generalized gradient approximation made simple. *Phys. Rev. Lett.* **77**, 3865–3868 (1996).
68. Nørskov, J. K. et al. Origin of the overpotential for oxygen reduction at a fuel-cell cathode. *J. Phys. Chem. B* **108**, 17886–17892 (2004).
69. Li, T., Yu, Y. & Pei, M. Dual-atom doping carbon materials as highly efficient electrocatalysts for lithium-sulfur batteries: bimetallic cooperation mechanism. *J. Phys. Chem. C.* **127**, 6271–6279 (2023).

Acknowledgements

This work was supported by grants from the National Natural Science Foundation of China (22471196, 22171214, H.F.), the Postdoctoral Fellowship Program of China Postdoctoral Science Foundation (GZC20241222, Y.J.), the Natural Science Foundation of Shanghai (22ZR1463200, H.F.), the Xiaomi Young Talents Program (H.F.), the Recruitment of Global Youth Experts by China (H.F.), the Fundamental Research Funds for the Central Universities (H.F.) and the Science & Technology Commission of Shanghai Municipality (19DZ2271500, H.F.).

Author contributions

Y.J., R.X., C.Z., and H.F. conceived the project. H.F. supervised the project, and Y.J. performed the major experimental studies. R.X. contributed to the photocatalyst synthesis, and J.Y. assisted in the crystallographic analysis. C.S., Y.L., and W.C. assisted in synthesis and photophysical studies. Y.J. and H.F. wrote and revised the manuscript. All authors contributed to the discussion and revisions.

Competing interests

The authors declare no competing interests.

Additional information

Supplementary information The online version contains supplementary material available at https://doi.org/10.1038/s41467-025-60954-4.

Correspondence and requests for materials should be addressed to Chi Zhang or Honghan Fei.

Peer review information *Nature Communications* thanks Bo Weng who co-reviewed with Shufen WangJiadong Xiao and the other, anonymous, reviewer for their contribution to the peer review of this work. A peer review file is available.